Frontiers of Information Technology & Electronic Engineering
www.jzus.zju.edu.cn; engineering.cae.cn; www.springerlink.com
ISSN 2095-9184 (print); ISSN 2095-9230 (online)
E-mail: jzus@zju.edu.cn

Electronically enhancing the long-range nanopositioning accuracy of a Lorentz force actuator*

Bimal Jeet GOTEEA, Qianjun ZHANG, Wei DONG‡

State Key Laboratory of Robotics and System, Harbin Institute of Technology, Harbin 150001, China

E-mail: bj.goteea@gmail.com; zhang_qj@stu.hit.edu.cn; dongwei@hit.edu.cn

Received June 12, 2022; Revision accepted Sept. 16, 2022; Crosschecked July 5, 2023

Abstract: This paper presents a precision centimeter-range positioner based on a Lorentz force actuator using flexure guides. An additional digital-to-analog converter and an operational amplifier (op amp) circuit together with a suitable controller are used to enhance the positioning accuracy to the nanometer level. First, a suitable coil is designed for the actuator based on the stiffness of the flexure guide model. The flexure mechanism and actuator performance are then verified with finite element analysis. Based on these, a means to enhance the positioning performance electronically is presented together with the control scheme. Finally, a prototype is fabricated, and the performance is evaluated. This positioner features a range of 10 mm with a resolution of 10 nm. The proposed scheme can be extended to other systems.

Key words: Nanopositioning; Flexure guides; Long range; Voice coil motor; Lorentz force actuator
https://doi.org/10.1631/FITEE.2200255 **CLC number:** TM36; TN710

1 Introduction

Electromagnetic actuators operating under the Lorentz force principle are often used in medium- to long-range precision positioning (Shan et al., 2015). Sample application domains include: *XY* precision positioning platforms of 10 mm range for biological sample manipulations (Leung et al., 2011), millimeter range positioning platforms (Lin R et al., 2019; Wang et al., 2021), micro assembly (Probst et al., 2009), optical alignment (Yang et al., 2022), high-performance automotive transmissions (Baronti et al., 2013), intake valve control for combustion engines (Mercorelli, 2017; Dimitrova et al., 2019; Gao et al., 2019), and magnetic levitations (Kim JY and Ahn, 2020). These actuators are ideal for such applications, as they offer backlash-free and cog-free motions with theoretically infinite resolution, as there is no contact between the stator and the mover. A classic example is the voice coil motor (VCM). Apart from these advantages, a precision platform employing such actuators can be affected by the excessive heat generated by the coil if it is not properly designed (Shan et al., 2015; Teo et al., 2015), and performance tradeoffs often need to be considered (Hiemstra et al., 2014). Additionally, the control of nanopositioning platforms leads to significant challenges as surveyed by Devasia et al. (2007).

For precision positioning, the motion must be adequately confined along a predefined axis by some form of guideway. Traditional contact-type linear bearings, although widespread, suffer from nonpredictable frictional forces and the stick-slip phenomenon, which become dominant over minute displacements, making nanopositioning challenging (Christiansen et al., 2008; Lin CJ et al., 2013; Takrouri and Dhaouadi, 2016). To circumvent these, noncontact guideways,

‡ Corresponding author
* Project supported by the National Key Research and Development Plan of China (No. 2017YFB1303101)
ORCID: Bimal Jeet GOTEEA, https://orcid.org/0000-0002-3101-1584; Qianjun ZHANG, https://orcid.org/0000-0002-9862-5695; Wei DONG, https://orcid.org/0000-0002-1211-6444
© Zhejiang University Press 2023

such as magnetic levitation (Kim WJ et al., 1998; Choi and Gweon, 2011; Zhu et al., 2019) and aerostatic bearings (Shinno and Hashizume, 2001; Tan et al., 2012), can be used; however, these guideways not only are costly and voluminous but also require additional control to compensate for the multiple degrees of freedom that they exhibit.

Flexure mechanisms, on the other hand, offer repeatable friction-free and backlash-free motions confined over a compliant axis for lower cost, making them ideal for precision positioning over short to medium ranges. They also have long service lives and are virtually maintenance-free, provided that the material is not deformed beyond its elastic limit and fatigue point (Howell, 2013). Recently, the potential of flexure mechanisms and electromagnetic actuators has been combined into a single unit, as in Teo et al. (2007) and Zhu et al. (2018), to offer nanometer resolution over a range of a few millimeters for embryonic and cell manipulations, micro/nano feature probing (Teo et al., 2010), and ultraviolet (UV) lithography processes (Teo et al., 2014).

Even though a Lorentz-based actuator has theoretically infinite resolution, it is difficult to achieve high resolution and long range simultaneously, as the performance also depends on the underlying subsystems, such as the drives, controllers, sensors, and to some extent the skills of the experimenter (Makarovic, 2006). This can be overcome using dual actuator stages configured in a macro-micro configuration (Sharon et al., 1993), which is usually heterogeneous in nature, combining actuators such as the VCM for long range and a lead zirconate tiranate (PZT) for short range (Dong et al., 2009) for a diamond polishing application, or a linear motor for long range and a VCM for short range for a precision table (Shinno and Hashizume, 2001) and an ultra-precision scanning system (Kim KH et al., 2006). The heterogeneous nature of these actuators usually complicates the control and assembly. Additionally, solutions relying on piezo stack actuators (PSAs) need to compensate for the complex hysteresis that they suffer from (Gu et al., 2016). There can also be homogeneous solutions, for example, in Cheung and Cheung (1997), where two individual VCMs were used back to back to form a macro-micro system for a wire bonding machine for semiconductor packaging. However, that system suffered from low stiffness and required complex control. Another means is to use a dual coil arrangement as done by Yoo and Kwon (2007), who achieved a range less than 35 μm for the macro coil and a resolution of 2 nm for the micro coil, for a nanolevel measurement system for the semiconductor industry. However, such configurations for precision positioning are infrequently reported. The problem with employing a micro coil is the additional space required to install it, which may or may not be available. Moreover, if additional space is allocated, in a traditional setup, the main coil will be placed further away from the magnets, which will tend to reduce the magnetic field strength that it experiences. Furthermore, for the micro coil, which is usually wound in the middle of the main coil to minimize magnetic interference, to be effective, it must translate within the length of the air gap, which might not be possible, especially if the main coil is overhung.

In this study, we propose a method to electronically create a micro coil to achieve low submicron root mean square error (RMSE) tracking for a centimeter range with 10 nm step resolution for a prototype one-dimensional (1D) positioner. The principle can be applied to multidegree-of-freedom (MDOF) positioners.

2 Mechanical, electromagnetic, and electronic design

2.1 Design of flexure mechanism

Based on the relatively small 48 mm diameter of the stator of the VCM, three multiple compound parallelogram flexures (MCPFs) arranged in parallel, as shown in Fig. 1, with motion directed in the x direction, are used for the guiding mechanism built on Pham and Chen (2005) and Xu (2012) for MCPFs.

The flexure can be decomposed into six beams that can be simplified by applying the fix-sliding model. Each beam is subjected to a combined moment (M), axial reaction force (R), and driving force (F), when force F_x is applied to the primary side of the flexure (Fig. 1a). This results in a statistically indeterminate beam, and with the appropriate boundary conditions, the resulting one-sided displacement Δx becomes $5\delta x+\delta x_1$, where δx is the displacement of the beam having length l and δx_1 is the displacement of the beam having length l_1. The motional stiffness (K) of the flexure

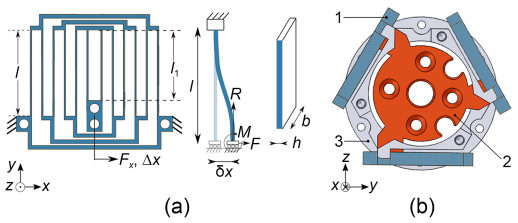

Fig. 1 Design of one flexure unit (a) and top view of the positioner with three flexures connected in parallel (b) (1: flexure unit; 2: motion platform (head); 3: flexure holder)

can be calculated based on the bending moment, $K=\frac{2F}{\Delta x}$, with $F=\frac{F_x}{2}$, $\delta x=\frac{Fl^3}{12EI}$, $\delta x_1=\frac{Fl_1^3}{12EI}$, and $I=\frac{bh^3}{12}$. Substituting these into K yields

$$K=\frac{2Ebh^3}{5l^3+l_1^3}, \tag{1}$$

in terms of the geometry and material properties of the flexure, where E is Young's modulus, I is the moment of inertia, b is the width, h is the thickness, and l and l_1 are the lengths of the flexure beams.

Aluminum 2A21 is used for the flexures, and it has a Young modulus of 70.6 GPa for a tensile strength of 470 MPa. The density is 2780 kg/m^3 and the Poisson ratio is 0.33.

For a compact design and to meet the desired stroke with the force produced by the VCM, a small work envelope is desired. The peak force for 1 A is estimated to be 9 N, and the desired one-sided translation is 5 mm. Based on the diameter of the VCM stator and coil bobbin, the following parameters of the flexure are determined: b=4 mm, l=22 mm, and l_1=18 mm. Substituting these into Eq. (1), h is calculated to be 0.39 mm, which is rounded to 0.4 mm owing to manufacturing constraints.

Each flexure has a calculated stiffness of 612 N/m, resulting in a theoretical stiffness of 1836 N/m (612×3) for the assembly, the margin of error of which is within 3.1% compared with 1781 N/m obtained by finite element analysis (FEA).

2.2 Design of the VCM coil

The objective is to design a coil capable of delivering at least 10 N/A to deform the flexures and produce the desired stroke. By having the force constant greater than the required force, a current consumption of less than 1 A will be needed, which results in less heat being generated by the coil due to Joules heating (I^2R), as the square of a number less than unity is smaller than the number itself. An existing stator made of six arc-shaped magnets is used to provide a near-uniform radial magnetic field perpendicular to the coil for the electromagnetic actuation scheme. The averaged magnetic field strength (B) in the air gap is 0.27 T. From the Lorentz force equation, $F=i\int \mathrm{d}L\times B$, which can be conveniently rewritten as $F=BIlN$, where F is the generated force, I is the current, l is the averaged circumference of the coil (30.5 mm), and N is the number of turns of the coil in the magnetic field which can be calculated. N is found to be 393 (~400) turns. For implementation, N is increased by 20% to 480 turns to ensure that the force constant will be at least 10 N/A as the magnetic field due to the six arc-shaped magnets is not entirely uniform due to magnetic fringing and assembly tolerances. With these 480 turns, the coil has an averaged indicative force constant of 12.6 N/A. The coil is wound with 0.35 mm enamel copper with a hexagonal winding pattern over four layers. The coil is current-driven, and based on the stiffness of the flexure assembly, the digital-to-analog converter (DAC) voltage output and resolution, and the transconductance of the current drive, an equation can be formulated to calculate the minimum open-loop displacement ($X_{\mathrm{min_open}}$) as follows:

$$X_{\mathrm{min_open}}=\frac{1}{K}\left(\frac{1}{2^{N_{\mathrm{bits}}}-1}\right)V_{\mathrm{DAC}}TK_{\mathrm{f}}, \tag{2}$$

where N_{bits} is the resolution of the DAC in bits, which is 16 in this case, V_{DAC} is half the voltage range of the bipolar DAC, which is 10 V, T is the transconductance of the linear current drive, which is 0.4 A/V, K_{f} is the indicative force constant of the VCM, and K is the stiffness of the flexure mechanism. Substituting the appropriate values, the minimum open-loop displacement is 864 nm. With suitable feedforward (FF) and feedback (FB) controllers, the resolution is at best 50 nm, as will be shown in Section 4.4.

2.3 Design of an electronic micro coil to overcome the positioning limitation of the actuator

The desired resolution of the system is 10 nm, and a means of increasing this resolution from 50 nm is needed. There are various ways of achieving this,

such as using another actuator in a macro-micro configuration to perform these small displacements, such as a PZT, or a micro coil. On the electronics side, a higher-resolution DAC can be employed. However, they all have their disadvantages. Adding another actuator requires physical space for the actuator and mounting fixtures, and this requires a different drive technology in case the actuation system becomes nonhomogeneous. To keep the system homogeneous, winding a micro coil is a feasible route, but it requires enough space in the air gap, and its efficacy depends on it being in the effective air gap over the whole stroke. Another linear current drive is needed, and the force generated by the micro coil needs to be properly characterized. Using a higher-resolution DAC has its own disadvantage, as such DACs are usually substantially more expensive and, depending on the manufacturer, they can suffer from integral nonlinearity (INL) and differential nonlinearity (DNL) noise up to four least significant bits (LSBs), which can make them perform worse than lower-resolution DACs.

However, the idea of using a micro coil is interesting, as it keeps the actuation system homogeneous. In this situation, the micro coil and the coil of the VCM (macro coil) each produces a force that adds up, due to the principle of superposition, to displace the flexures and cause the required displacement. The micro coil is made to produce small corrective forces that the macro coil cannot produce due to the resolution of the voltage (V_{Drive}) used to drive its current amplifier. Based on the principle of superposition and the fact that the coils are to be current-driven with linear transconductace amplifiers, the micro coil can be emulated electronically.

The desired open-loop resolution is 20 nm as the displacement will be measured with 10 nm resolution. Based on Eq. (2), such a resolution per DAC LSB requires the micro coil should have an indicative force constant of 0.29 N/A for a 16-bit DAC, and if realized, it would require approximately 12 turns. This implies that the micro coil will use 43.4 (12.6/0.29) times more current to produce the same force, effectively increasing the resolution at which the force can be generated. We implement this coil with a set of operational amplifiers (op amps) and an additional DAC. For the rest of this paper, this coil and its associated subsystem will be called the electronic coil. Since the same linear current drive and a similar resolution DAC are being used, this ratio is equal to that of the actual open-loop resolution to the desired open-loop resolution:

$$A=\frac{x_{\mathrm{a}}}{x_{\mathrm{d}}}, \tag{3}$$

where A is the amplification factor, x_{a} is the actual resolution, and x_{d} is the desired resolution. This scheme is implemented using the electronic circuit shown in Fig. 2.

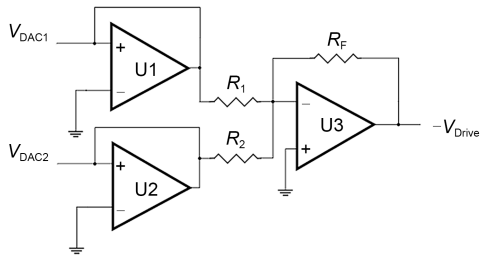

Fig. 2 Schematic of the summing circuit

The circuit comprises three op amps: U1 and U2 are used as voltage followers to buffer the output voltages of the two DACs (V_{DAC1} and V_{DAC2}) and the final op amp, and U3 is configured as an inverting summing amplifier that scales and adds these two voltages to produce the final drive voltage V_{Drive}. This is equivalent to summing the two coil currents.

With respect to the controller in Section 3.3, V_{DAC1} is responsible for reproducing the force commanded for the coil by the main FF and FB controllers. As such, it is only buffered. The drive voltage, V_{DAC2}, for the electronic coil, on the other hand, is amplified in software by factor A and is outputted via the second DAC, which can then reproduce it properly. Once outputted, it has to be converted back to its original magnitude. This is done by the resistor pair R_{F}/R_2 of U3, which attenuates the drive voltage by factor A once it has been buffered by U2.

A negation of the voltage outputs of the DACs is performed in software to produce the correct output. The choice of the op amps is important in that they must exhibit the least null-offset voltage (error) as much as possible as they multiply and sum the voltages, and any offset will produce a nonlinear output. For the implementation, the AD817 is chosen because

it has a high-bandwidth and high-precision op amp with a null offset trim functionality. This allows the output of each op amp to be trimmed to 0 V when the inputs are zero and to minimize disturbance d_7 (Section 3.3). The op amps are powered with a standard ±15 V to allow the output to follow the ±10 V DAC output. Although the desired attenuation factor is 43, this ratio is conveniently set to 47 based on standard resistor values with 1% tolerance by having R_2=470 kΩ and R_F=10 kΩ. R_1 is set to 10 kΩ to produce unity gain, and the final drive voltage is given by Eq. (4):

$$V_{\text{Drive}}=-V_{\text{DAC1}}\frac{R_{\text{F}}}{R_1}-V_{\text{DAC2}}\frac{R_{\text{F}}}{R_2}, \tag{4}$$

with $\frac{R_{\text{F}}}{R_1}=1$ and $\frac{R_{\text{F}}}{R_2}=\frac{1}{A}=\frac{1}{47}$.

2.4 Finite element analysis force simulation

A three-dimensional (3D) magnetostatic FEA simulation is carried out for the generated force by the VCM with currents of ±0.5, ±1, ±2, and ±3 A. The results are shown in Fig. 3a and the resulting pushing and pulling force constants shown in Fig. 3b. The following materials are used for the simulation: NdFeB42 for the magnets, carbon steel 1020 for the motor case, back plate, outer casing and center pole, and aluminum 6061 for the custom bobbin copper for the coil. These are best guesstimates of the ones used by the manufacturer. The bulk of the pushing and pulling forces is due to the Lorentz force, and the remaining forces are due to magnetic attraction and repulsion, which are inherent to the motor structure. A two-dimensional (2D) magnetostatic axis symmetry FEA simulation, although computationally less demanding, is not performed, as it would have modeled the six arc-shaped magnets as a hollow cylinder, resulting in the simulated force being greater due to the increase in magnetic volume and decrease in magnetic fringing.

As seen in Figs. 3a and 3b, the pushing and pulling forces for a given current are not the same, and their magnitudes vary along the stroke. This is due to the magnetic field generated by the current flowing into the coil interacting with that flowing into the center pole due to the permanent magnets. The normalized magnetic field flowing into the center pole at a distance of 7.87 mm from the centerline (which is incidentally in the middle of the metal portion of the latter) is shown in Fig. 3c. This explains the shape of the pushing and pulling force curves. As the direction of this magnetic field is set by the permanent magnets, it will either attract or repel the one setup in the coil due to current. These forces are near horizontal mirror images of each other about the averaged force constant. In addition, the magnetic field generated by the coil is attracted to the back plate, causing a decrease in the pushing force but an equivalent increase in the pulling force. There is also magnetic saturation of the iron in the motor when high currents are used, as seen in the increasing gap between the pushing and pulling forces in Fig. 3a.

The force simulation shows an average force constant of 12.4 N/A, which is slightly lower than that theoretically calculated (12.6 N/A). This force constant also ensures that less than 1 A will be required to produce a maximum stroke of ±5 mm.

2.5 Assembly

The assembly is made of aluminum 6061 with the exception of the flexures and head (Fig. 4b). Nonmagnetic fasteners and fixtures are used to minimize

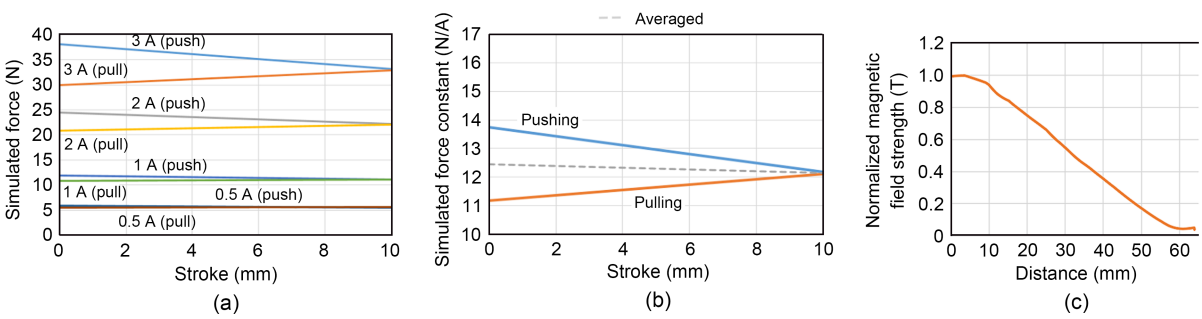

Fig. 3 Simulated force generated by the coil (a), the resulting simulated force constant (b), and the normalized magnetic field strength in the center pole (c) (References to color refer to the online version of this figure)

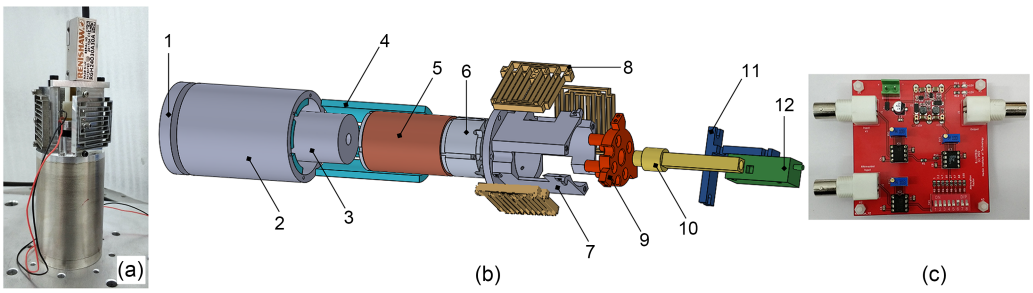

Fig. 4 Realized positioner (a), exploded view of the positioner (b), and the summing amplifier board (c) (1: back plate; 2: motor case; 3: center pole; 4: arc-shaped magnets (×6); 5: coil; 6: bobbin; 7: flexure assembly holder; 8: flexures (×3); 9: head; 10: encoder ruler holder; 11: encoder holder; 12: encoder)

the magnetic interference. Special considerations are given to allow air trapped between the inner surface of the bobbin and the center pole to escape to minimize damping, especially at 10 Hz reciprocating motions. For cable management, the assembly features cut-in slots to allow the exit of the multistrand pure copper wires with a supple silicone coating to minimize wire-induced disturbances, which can be significant, as in Devasia et al. (2007) and Hiemstra et al. (2014), for nanopositioning based on moving coil actuators. A noncontacting linear incremental encoder is used for displacement measurement, as it is robust and has good noise immunity. These together minimize the disturbances on the positioner.

The flexure assembly has a measured stiffness of 1655 N/m, which is within 7.1% of the FEA value. According to FEA, the maximum von-Misses stress in the flexures is 158.41 MPa and based on the 0.2% yield strength of 325 MPa for aluminum 2A21, the assembly has a respectable safety factor of 2.05.

The harmonic behavior of the system is investigated through the first five vibration modes obtained from FEA. The first two modes occur at 23.37 and 117.47 Hz, respectively; as seen in Fig. 5, the deformation is mostly contained along the axis of motion,

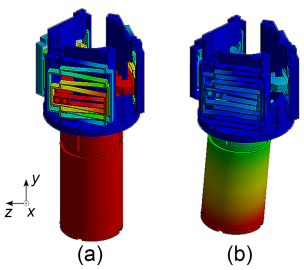

Fig. 5 First two vibration modes with motion in the *y* direction: (a) 23.37 Hz; (b) 117.47 Hz

making the system suitable for nanopositioning where the operating frequency is typically less than 10 Hz. The remaining vibration modes occur at 122.14, 203.5, and 203.5 Hz.

3 Electrical parameters, force constant, controller design, and op amp circuit

3.1 Electrical parameters and current drive transconductance

The 480-turn coil has a resistance of 11.9 Ω and an inductance of 1.060 mH, resulting in a cut-off frequency $R/(2\pi L)$ of 1.787 kHz. The linear current drive used has an output current (I) to input voltage (V) relationship of I=0.4217V−0.005 instead of the ideal transconductance of 0.4 A/V and has a bandwidth of 5 kHz. Based on these results, the sampling and actuation frequency of the controller is set to 1 kHz.

3.2 Force constant

The actual force constant of the VCM is measured using a T310-50N sensor with a T098H0-10V bridge amplifier from Right Co., Ltd. As expected, the pushing and pulling forces are not the same, and they vary along the stroke, as shown in Fig. 6a. The averaged measured force constant is 7% higher than the calculated value (13.5 N/A vs. 12.6 N/A) in Section 2.2 and is 8.9% higher than the averaged FEA force simulation (12.4 N/A) in Section 2.4. This validates the calculations and the electromagnetic FEA simulation. These discrepancies can be due to measurement errors and an uneven magnetic field in the air gap due to minute assembly errors when gluing the magnets and differences in the magnetic material properties.

A force-to-current block is used to equalize the pulling and pushing forces by calculating the required current to reproduce the desired force by the VCM by taking into account the stroke and the appropriate pushing or pulling force constant. The importance of this block can be seen in Figs. 6b and 6c, which compare the tracking of a 2.5-mm 1-Hz sinusoidal reference with the coil and electronic coil with and without compensating for the uneven pushing and pulling forces along the stroke. When this block is removed, the average K_f (13.5 N/A) is used instead. The proportional-integral-derivative (PID) values and A are as given in Section 4.2. The RMSE is 0.104 μm with the block in place, and 3.775 μm without it; the corresponding maximum absolute errors (MAXEs) are 0.2937 and 10.37 μm, respectively. These errors are orders of magnitude different. Additionally, the shape of the error curve is of interest. Without this block, one can see large errors when the motion reverses and the force changes from a pulling one to a pushing one, and vice versa. This is a major contributor to tracking errors.

3.3 Controller design

The controller schematic is shown in Fig. 7. The main controller consists of an FF controller and a PID FB controller to drive the coil of the VCM. The bulk of the positioning is performed by the FF controller, and discrepancies are reduced with the PID controller. These track a reference signal, r, and produce a force command, which is then converted into a current via a force-to-current block, which compensates for the variation in the pushing and pulling forces in the VCM. This current command is finally converted into a drive voltage via a current-to-voltage block, which compensates for the nonideal behavior of the linear current drive. These two blocks are imperative to make the system as linear time invariant (LTI) as possible, and they are the inverse models of the actual hardware. This drive voltage is then generated by a DAC card (NI 6229, 16-bit), which outputs a drive voltage within ±10 V, which is then fed into a linear current drive (Trust Automation, TA115). The latter converts

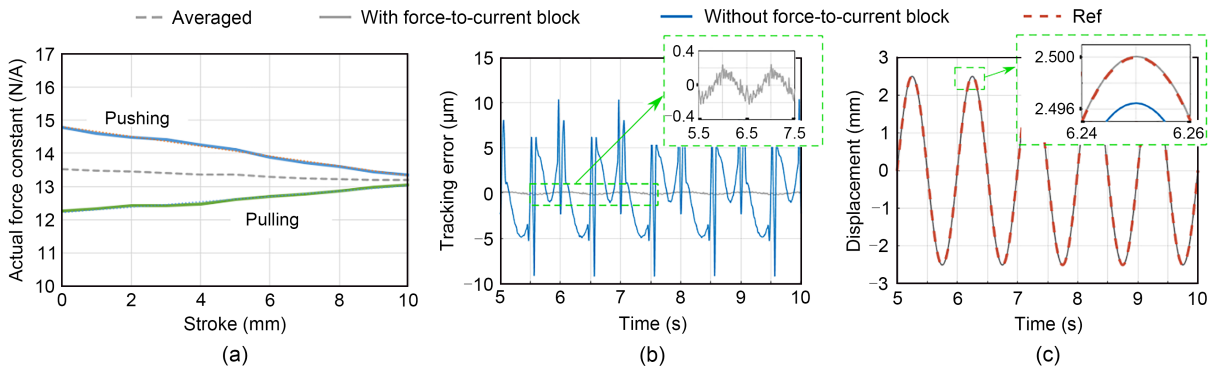

Fig. 6 Actual force constant of the actuator (a), tracking error with and without the force-to-current block (b), and tracking displacement with and without the force-to-current block (c) (References to color refer to the online version of this figure)

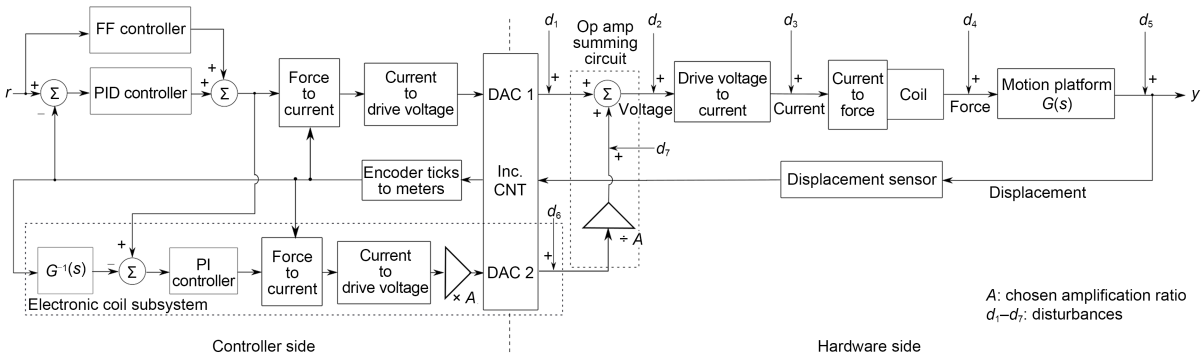

Fig. 7 Controller schematic (FF: feedforward; PID: proportional-integral-derivative; PI: proportional-integral; DAC: digital-to-analog converter)

this voltage into a current in the range of ±4 A, which the coil then converts into a force that displaces the positioner due to the stiffness of the flexures. This displacement (y) is measured with a linear incremental encoder (Renishaw RG24O series with 10 nm resolution). The current drive is powered by a linear power supply (Uni-T, UTP8305B). This displacement is influenced by parameter uncertainties and external disturbances d_1 to d_7, where d_1 and d_6 are primarily due to the resolution of the DACs, d_3 is any electrical noise in the power supply of the current drive and noise in the current drive itself, such as the Johnson noise, due to heating of the active components, d_4 is due to parameter uncertainties in the force constant of the VCM, and d_5 is mostly due to environmental noise, which makes it through the vibration isolation table QD01 (Lyseiki Co., Ltd., Beijing, China). These disturbances are usually small.

The measured displacement is converted into a force via a G^{-1}(s) block, which is the inverse model of the positioner. This force is compared with the commanded force by the FF and FB controllers for the coil. Any discrepancy between these two is due to disturbances and parameter uncertainties. This force discrepancy is then fed into a proportional-integral (PI) FB controller. This commanded force is then converted to an appropriate drive voltage after going through the force-to-current block and the current-to-drive voltage block. These blocks are identical to the aforementioned blocks, as the same coil and current drive are used. However, since this force discrepancy is small, as it has already been previously reduced by the FF and FB controllers, the output drive voltage by the DAC is small. This output voltage is amplified by a factor A in the software before being outputted by a second 16-bit DAC, which also produces a disturbance d_6. The op amp buffering and summing circuit first attenuates this drive voltage signal by the same factor A to restore it and adds it with that of the coil drive voltage from the first DAC. This scheme effectively overcomes these disturbances. The op amps will also introduce minute disturbances d_2 and d_7 due to any offset error or noise in the op amps.

Although the feedback control for the electronic coil resembles that of a disturbance observer (DOB), it is not the same as it does not use a Q filter. The disturbance is fed to a PI controller. There are two reasons for this: (1) The Q filter is difficult to build for a nonminimal phase system (Lee and Tomizuka, 1996); (2) The Q filter acts as a low-pass filter and attenuates the high-frequency noise, which needs to be suppressed by the electronic coil. These high-frequency noises are due to the quantization of the reference signal and tracking when the trajectory is near the encoder resolution. Removing these prematurely degrades the performance.

The Z transform is used to implement the FF controller $u_{\mathrm{ff}}(k)$, plant inverse $G^{-1}(s)$, and PID FB controller $u_{\mathrm{pid}}(k)$. These are defined as follows:

$$\begin{cases} u_{\mathrm{ff}}(k)=\left(m\dfrac{z-2}{T_{\mathrm{s}}Z}+c\dfrac{z-1}{T_{\mathrm{s}}Z}+k_{\mathrm{s}}\right)x_k, \\ u_{\mathrm{pid}}(k)=K_{\mathrm{p}}\left(1+K_{\mathrm{i}}T_{\mathrm{s}}\dfrac{1}{z-1}+K_{\mathrm{d}}\dfrac{N}{1+NT_{\mathrm{s}}\dfrac{1}{z-1}}\right)e_k. \end{cases}$$

The FF controller and the plant inverse G^{-1}(s) are identical. T_{s} is the sampling time of the controller, m, c, and k_{s} are the mass, damping coefficient, and spring coefficient, respectively, K_{p}, K_{i}, and K_{d} are the usual PID coefficients, N is the filter coefficient for the derivative calculations, x_k is the displacement at sample k, and e_k is the tracking error given by x_k-r_k with r being the reference trajectory.

4 Experimental performance evaluation

4.1 System identification

The transfer function of the displacement at the positioning stage was identified with respect to the applied force following the mass–spring–damper dynamic model $ik_{\mathrm{f}}=m\ddot{x}+c\dot{x}+k_{\mathrm{s}}x$, where m is the motional mass, c is the damping coefficient, k_{s} is the stiffness of the flexure mechanism, x, $\dot{x}$, and $\ddot{x}$ are the displacement, velocity, and acceleration, respectively, k_{f} is the force constant of the VCM, and i is the applied current. A force swept sine wave of 0.1 N amplitude and 0.1 to 100 Hz frequency was generated and applied by the actuator. The identified parameters were as follows: m=0.085 kg (actual mass 0.089 kg), damping coefficient c=9.243 N·s/m, and spring coefficient k_{s}= 1691 N/m (measured 1650 N/m). The calculated natural frequency at the positioning stage was 22.45 Hz

(theoretically 23.29 Hz). The transfer function had a fitting of 93.4%, as given in Eq. (5) with the phase and magnitude responses shown in Fig. 8:

$$\mathrm{TF}=\frac{11.76}{s^2+108.7s+18\,720}. \tag{5}$$

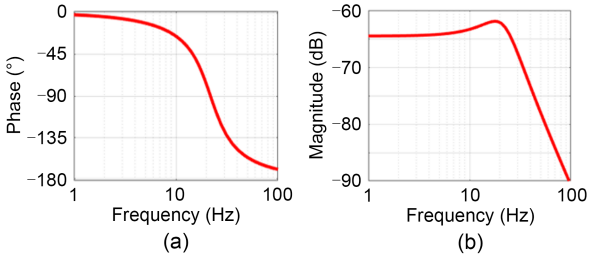

Fig. 8 Phase (a) and magnitude (b) responses at the positioning stage with respect to the applied force

4.2 Tracking of sinusoidal references

The PID values were as follows: for all 1 Hz experiments, K_p=15, K_i=11 500, and K_d=1. For 5 Hz and 10 Hz, K_p was increased to 125 and 175, respectively, to compensate for the phase lag. The PID values for the electronic coil were kept at K_p=1, K_i=19, and K_d=0 for all experiments. The amplification factor A was set to 47. The submillimeter tracking performance of the system was measured by following sinusoidal references of amplitude 0.5 mm with frequencies of 1, 5, and 10 Hz, as shown in Fig. 9. For large-range performance, 1.0, 2.5, and 5.0 mm sinusoidal references at 1 Hz were tacked and plotted, as shown in Fig. 10. The performance indices were RMSE and MAXE, which are defined as follows:

$$\begin{cases} \mathrm{RMSE} = \sqrt{\dfrac{1}{N}\sum_{i=1}^{N} e_i^2}, \\ \mathrm{MAXE} = \max\left(\left|e_i\right|\right). \end{cases}$$

The results are compiled in Table 1.

4.3 Step response

The step response of the positioner was investigated by following a 5-mm step reference modified to a 0.0625 m/s ramp to accommodate the maximum tracking velocity of 0.065 m/s of the RGH24Ox series of linear encoders. Without the electronic coil, the main error band was ±50 nm, and with it, the error band

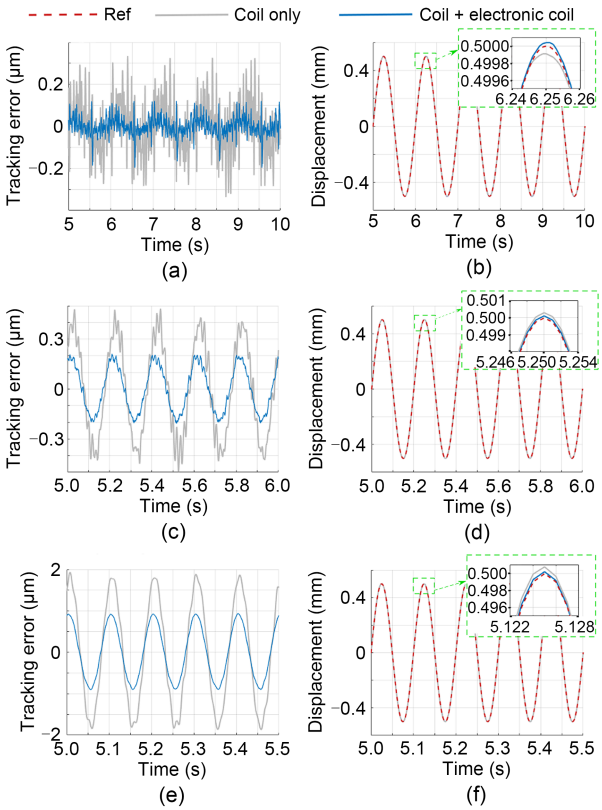

Fig. 9 Tracking error for 1 Hz (a), 5 Hz (c), and 10 Hz (e) for following sinusoidal references of 0.5 mm amplitude; tracking displacement for 1 Hz (b), 5 Hz (d), and 10 Hz (f) for following sinusoidal references of 0.5 mm amplitude

was reduced to ±10 nm, as seen in Fig. 11 together with the low-pass filtered displacement.

4.4 Resolution and validation of amplification factor *A*

The resolution was 10 nm with the electronic coil and 50 nm without it, as shown in Fig. 12.

As a means of validating the choice of A, an experiment was conducted with A set to 1, 2.2, 4.7, 10, 27, 47, 68, and 100, and the corresponding RMSEs for 10-nm resolution tracking were measured and plotted. As shown in Fig. 13, the RMSE falled logarithmically to 5 nm as A reached 47 and thereafter decreased marginally as the resolution of the encoder and environmental disturbances became dominant.

4.5 Random trajectory tracking

To test the generality of the controller and actuator, a random path was generated and tracked with and without the electronic coil, as shown in Fig. 14.

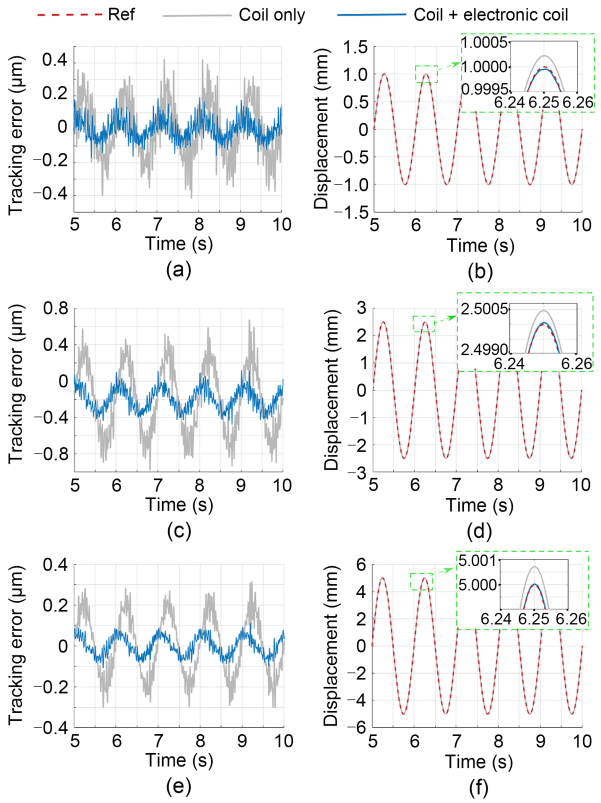

Fig. 10 Tracking error for 1 mm (a), 2.5 mm (c), and 5 mm (e) at 1 Hz; tracking displacement for 1 mm (b), 2.5 mm (d), and 5 mm (f) at 1 Hz

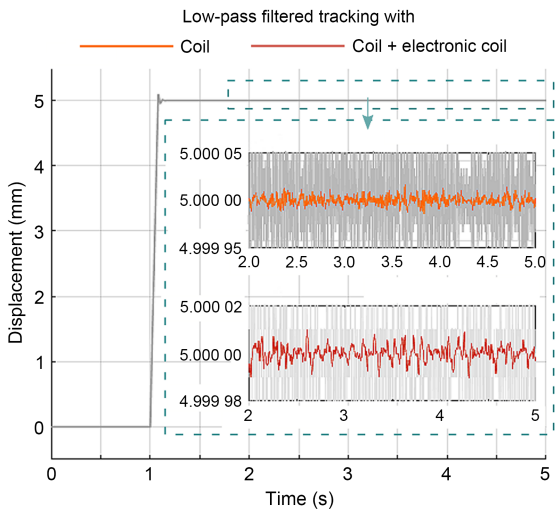

Fig. 11 Tracking with a 5-mm step (References to color refer to the online version of this figure)

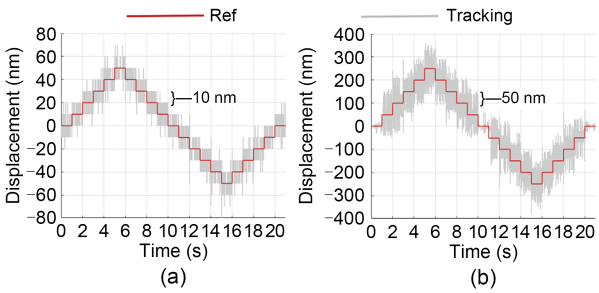

Fig. 12 Resolution: (a) with coil and electronic coil; (b) with coil only

The PID values and A were set as given in Section 4.2. The RMSE was 0.1331 μm without the electronic coil and 0.0631 μm with it, while the MAXE was 0.5970 μm without the electronic coil and 0.3057 μm with it.

5 Discussion, comparison, and conclusions

5.1 Discussion

The resulting mechanical assembly was relatively compact, as it was slightly larger than the diameter of the VCM. It had a stiffness within 10% of the theoretical value and FEA simulation results and allowed tracking of up to 10 Hz, with the first vibration mode occurring at 23.37 Hz. The assembly also offered a relatively high safety factor of 2.05. Additionally, the theoretical stiffness of the flexure was within 3.1% of the FEA result. The averaged force of the VCM was within 9% of the theoretical value and electromagnetic FEA simulations.

Table 1 Root mean square error (RMSE) and maximum absolute error (MAXE) with and without an operational amplifier

Stroke (mm)	Frequency (Hz)	RMSE (μm)		MAXE (μm)	
		Coil only	Coil + electronic coil	Coil only	Coil + electronic coil
0.5	1	0.119	0.043 (63.9%)	0.394	0.207 (47.5%)
0.5	5	0.280	0.134 (52.1%)	0.547	0.228 (58.3%)
0.5	10	1.280	0.637 (50.2%)	2.010	0.939 (53.3%)
1.0	1	0.166	0.061 (63.3%)	0.555	0.234 (57.8%)
2.5	1	0.357	0.117 (67.2%)	0.889	0.312 (64.9%)
5.0	1	0.732	0.226 (69.1%)	1.700	0.561 (67.0%)

Percentage improvements with the operational amplifier are shown in brackets

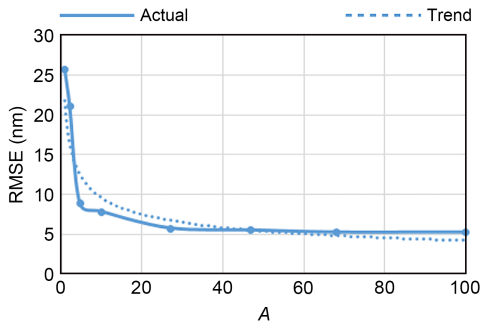

Fig. 13 Root mean square error (RMSE) for 10-nm resolution tracking with varying amplification factor *A*

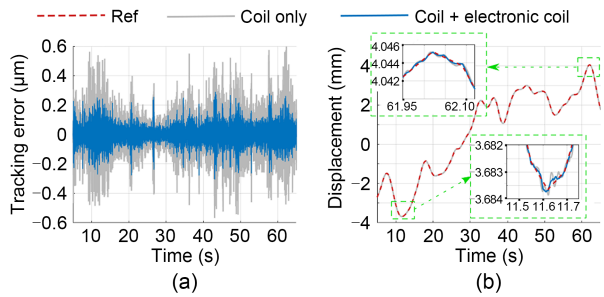

Fig. 14 Tracking error for a random path (a) and tracking of the random path (b)

The tracking performance results showed that the RMSE for sinusoidal trajectories can be reduced by 50% to 69% depending on the amplitude and frequency, while the MAXE can be reduced by 47% to 67%, as seen in Table 1. With the electronic coil, the RMSE was kept well below 1 μm, while the MAXE was below 1 μm for all trajectory tracking. The MAXE was more sensitive to environmental disturbances. The resolution was improved fivefold from 50 nm to 10 nm, which was also evidenced by the 5-mm step trajectory tracking where the error band was reduced from ±50 nm to ±10 nm. When the system was made to track a random path, the RMSE was reduced by 52.6%, while the MAXE was reduced by 48.8%. These results showed the effectiveness of the use of the electronic coil and the controller in enhancing long-range nanopositioning performance (accuracy) without resorting to an additional physical micro actuator. Additionally, the optimal amplification factor A was verified experimentally.

Such performance is feasible if the system is as LTI as possible. One major contributor to nonideal behavior is the difference in the pushing and pulling forces generated by the VCM due to magnetic attraction and repulsion, which is inherent to VCM construction. The discrepancy in current drive transconductance must also be accounted for. Although not shown, this discrepancy is easily visible in resolution tracking, especially when the commanded displacement is zero. Additionally, care must be taken in minimizing external disturbances, such as those due to the stiffness of the wires, especially for submillimeter displacements. With everything being equal, the RMSE for tracking a 2.5-mm 1-Hz sinusoidal reference showed a reduction to 1/36, and the MAXE showed a reduction to 1/35 when the hysteresis and nonlinearity in the force were compensated for. Once the system was LTI, it relaxes the requirements for a sophisticated controller such that FF and PID FB and PI controllers proved sufficient.

This method is suitable for linear current drives without a dead band and for most commercially available VCMs, including those using an axial magnet with a flux pole that oriented the magnetic field into the air gap. Such VCMs usually have overhung coils; that is, they are longer than the effective air gap, and retrofitting a micro coil is not a viable option because once it moves out of the air gap, it loses its effectiveness. Additionally, because the volume of the coil is much larger than that of a hypothetical micro coil, it is less affected by small variations in the magnetic field, which ensures more uniform force generation. Based on Eq. (2), a lower-resolution DAC can be used for the electronic coil, which can reduce the implementation cost.

5.2 Comparison with previous works

The performance of this system with respect to resolution and stroke is comparable to if not better than those of other positioning systems employing the VCM and flexure mechanisms, as seen in Table 2. The natural frequency of the system is sufficient for nanopositioning, which is usually less than 10 Hz.

This system also compares favorably with a recent state-of-the-art positioning system using annual flexure guides and a VCM for precision optics. That system used a 20-bit DAC with a 10-kHz sampling rate, and the VCM had a nominal force constant of 24 N/A. The controller used was a similar FF and PID control (Yang et al., 2022). The tracking performance comparison is summarized in Table 3. The performance improvements are appreciable even without the electronic coil.

Table 2 Comparison with previous works

Reference	Stroke (mm)	Resolution		Natural frequency (Hz)
		Value (nm)	Percentage of stroke (%)	
Hiemstra et al. (2014)	10	20	0.0002	25.00
Xu (2013)	11	250	0.0023	23.40
Xu (2014)	11	200	0.0018	29.30
Yang et al. (2022)	10	20	0.0002	38.99
This work	10	10	0.0001	22.45

Table 3 Comparison of sinusoidal tracking performance with Yang et al. (2022)

Frequency (Hz)	Stroke (mm)	Improvement by this work (%)			
		Coil		Coil + electronic coil	
		RMSE	MAXE	RMSE	MAXE
5	0.5	48.7	42.3	75.2	76.0
10	0.5	23.9	17.4	62.1	61.3
1	1.0	20.0	33.7	79.1	65.2
1	5.0	52.5	35.8	85.3	78.8

5.3 Conclusions

The proposed actuator and positioner are suitable for nanopositioning over a ±5 mm stroke with a 10-nm resolution. The importance of suppressing nonlinearity in the force was also demonstrated. The electronic coil and associated controller proved effective in substantially reducing the tracking errors, and the performance compared favorably with those of the recently proposed positioning systems.

Currently, a more sophisticated controller capable of automatically compensating for the phase lag is being investigated.

Contributors

Bimal Jeet GOTEEA designed the experiment, processed the data, and drafted the paper. Wei DONG supervised the research and contributed to funding acquisition. Qianjun ZHANG and Wei DONG revised and finalized the paper.

Compliance with ethics guidelines

Wei DONG is a corresponding expert of *Frontiers of Information Technology & Electronic Engineering*. Bimal Jeet GOTEEA, Qianjun ZHANG, and Wei DONG declare that they have no conflict of interest.

Data availability

The data that support the findings of this study are available from the first author upon reasonable request.

References

Baronti F, Lazzeri A, Roncella R, et al., 2013. Design and characterization of a robotized gearbox system based on voice coil actuators for a Formula SAE race car. *IEEE/ASME Trans Mechatron*, 18(1):53-61. https://doi.org/10.1109/TMECH.2011.2162632

Cheung NC, Cheung BMY, 1997. Modelling and control of a high speed, long travel, dual voice coil actuator. Proc 2nd Int Conf on Power Electronics and Drive Systems, p.270-274. https://doi.org/10.1109/PEDS.1997.618715

Choi YM, Gweon DG, 2011. A high-precision dual-servo stage using Halbach linear active magnetic bearings. *IEEE/ASME Trans Mechatron*, 16(5):925-931. https://doi.org/10.1109/TMECH.2010.2056694

Christiansen B, Maurer H, Zirn O, 2008. Optimal control of a voice-coil-motor with coulombic friction. Proc 47th IEEE Conf on Decision and Control, p.1557-1562. https://doi.org/10.1109/CDC.2008.4739025

Devasia S, Eleftheriou E, Moheimani SOR, 2007. A survey of control issues in nanopositioning. *IEEE Trans Contr Syst Technol*, 15(5):802-823. https://doi.org/10.1109/TCST.2007.903345

Dimitrova Z, Tari M, Lanusse P, et al., 2019. Robust control for an electromagnetic actuator for a camless engine. *Mechatronics*, 57:109-128. https://doi.org/10.1016/j.mechatronics.2018.12.004

Dong W, Tang J, ElDeeb Y, 2009. Design of a linear-motion dual-stage actuation system for precision control. *Smart Mater Struct*, 18(9):095035. https://doi.org/10.1088/0964-1726/18/9/095035

Gao HL, Zhang FJ, Wang EH, et al., 2019. Optimization and simulation of a voice coil motor for fuel injectors of two-stroke aviation piston engine. *Adv Mech Eng*, 11(4):1-17. https://doi.org/10.1177/1687814019846261

Gu GY, Zhu LM, Su CY, et al., 2016. Modeling and control of piezo-actuated nanopositioning stages: a survey. *IEEE Trans Autom Sci Eng*, 13(1):313-332. https://doi.org/10.1109/TASE.2014.2352364

Hiemstra DB, Parmar G, Awtar S, 2014. Performance tradeoffs posed by moving magnet actuators in flexure-based nanopositioning. *IEEE/ASME Trans Mechatron*, 19(1):201-212. https://doi.org/10.1109/TMECH.2012.2226738

Howell LL, 2013. Compliant mechanisms. Proc 21st Century Kinematics, p.189-216. https://doi.org/10.1007/978-1-4471-4510-3_7

Kim JY, Ahn D, 2020. Analysis of high force voice coil motors for magnetic levitation. *Actuators*, 9(4):133. https://doi.org/10.3390/act9040133

Kim KH, Choi YM, Gweon DG, et al., 2006. Design of decoupled dual servo stage with voice coil motor and linear motor for *XY* long stroke ultra-precision scanning system. *Proc SPIE*, 6040:60401C. https://doi.org/10.1117/12.664218

Kim WJ, Trumper DL, Lang JH, 1998. Modeling and vector control of planar magnetic levitator. *IEEE Trans Ind Appl*, 34(6):1254-1262. https://doi.org/10.1109/28.738999

Lee HS, Tomizuka M, 1996. Robust motion controller design

for high-accuracy positioning systems. *IEEE Trans Ind Electron*, 43(1):48-55. https://doi.org/10.1109/41.481407

Leung C, Lu Z, Esfandiari N, et al., 2011. Automated sperm immobilization for intracytoplasmic sperm injection. *IEEE Trans Biomed Eng*, 58(4):935-942. https://doi.org/10.1109/TBME.2010.2098875

Lin CJ, Yau HT, Tian YC, 2013. Identification and compensation of nonlinear friction characteristics and precision control for a linear motor stage. *IEEE/ASME Trans Mechatron*, 18(4): 1385-1396. https://doi.org/10.1109/TMECH.2012.2202679

Lin R, Li YZ, Zhang YX, et al., 2019. Design of a flexure-based mixed-kinematic *XY* high-precision positioning platform with large range. *Mech Mach Theory*, 142: 103609. https://doi.org/10.1016/j.mechmachtheory.2019.103609

Makarovic J, 2006. Lightweight Positioning: Design and Optimization of an Actuator with Two Controlled Degrees of Freedom. PhD Thesis, Technische Universiteit Eindhoven, Eindhoven, the Netherlands.

Mercorelli P, 2017. A motion-sensorless control for intake valves in combustion engines. *IEEE Trans Ind Electron*, 64(4): 3402-3412. https://doi.org/10.1109/tie.2016.2598314

Pham HH, Chen IM, 2005. Stiffness modeling of flexure parallel mechanism. *Prec Eng*, 29(4):467-478. https://doi.org/10.1016/j.precisioneng.2004.12.006

Probst M, Fluckiger M, Pané S, et al., 2009. Manufacturing of a hybrid acoustic transmitter using an advanced micro-assembly system. *IEEE Trans Ind Electron*, 56(7):2657-2666. https://doi.org/10.1109/TIE.2009.2021173

Shan GQ, Li YZ, Zhang LW, et al., 2015. Contributed review: application of voice coil motors in high-precision positioning stages with large travel ranges. *Rev Sci Instrum*, 86(10):101501. https://doi.org/10.1063/1.4932580

Sharon A, Hogan N, Hardt DE, 1993. The macro/micro manipulator: an improved architecture for robot control. *Robot Comput Integr Manuf*, 10(3):209-222. https://doi.org/10.1016/0736-5845(93)90056-P

Shinno H, Hashizume H, 2001. High speed nanometer positioning using a hybrid linear motor. *CIRP Ann*, 50(1):243-246. https://doi.org/10.1016/S0007-8506(07)62114-3

Takrouri M, Dhaouadi R, 2016. ADALINE-based friction identification of a linear voice coil DC motor. Proc American Control Conf, p.3062-3068. https://doi.org/10.1109/ACC.2016.7525386

Tan KK, Huang SN, Liang WY, et al., 2012. Development of a spherical air bearing positioning system. *IEEE Trans Ind Electron*, 59(9):3501-3509. https://doi.org/10.1109/TIE.2011.2171179

Teo TJ, Chen IM, Yang GL, et al., 2007. Magnetic field modeling of a dual-magnet configuration. *J Appl Phys*, 102(7): 074924. https://doi.org/10.1063/1.2794855

Teo TJ, Chen IM, Kiew CM, et al., 2010. Model-based control of a high-precision imprinting actuator for micro-channel fabrications. Proc IEEE Int Conf on Robotics and Automation, p.3159-3164. https://doi.org/10.1109/ROBOT.2010.5509145

Teo TJ, Yang GL, Chen IM, 2014. A large deflection and high payload flexure-based parallel manipulator for UV nano-imprint lithography: Part I. Modeling and analyses. *Prec Eng*, 38(4):861-871. https://doi.org/10.1016/j.precisioneng.2014.05.003

Teo TJ, Bui VP, Yang G, et al., 2015. Millimeters-stroke nanopositioning actuator with high positioning and thermal stability. *IEEE/ASME Trans Mechatron*, 20(6):2813-2823. https://doi.org/10.1109/TMECH.2015.2417776

Wang TW, Li YZ, Zhang YX, et al., 2021. Design of a flexure-based parallel *XY* micropositioning stage with millimeter workspace and high bandwidth. *Sens Actuat A Phys*, 331: 112899. https://doi.org/10.1016/j.sna.2021.112899

Xu QS, 2012. New flexure parallel-kinematic micropositioning system with large workspace. *IEEE Trans Rob*, 28(2): 478-491. https://doi.org/10.1109/TRO.2011.2173853

Xu QS, 2013. Design, testing and precision control of a novel long-stroke flexure micropositioning system. *Mech Mach Theory*, 70:209-224. https://doi.org/10.1016/j.mechmachtheory.2013.07.016

Xu QS, 2014. Design and development of a compact flexure-based *XY* precision positioning system with centimeter range. *IEEE Trans Ind Electron*, 61(2):893-903. https://doi.org/10.1109/TIE.2013.2257139

Yang M, Zhang C, Huang XL, et al., 2022. A long-stroke nanopositioning stage with annular flexure guides. *IEEE/ASME Trans Mechatron*, 27(3):1570-1581. https://doi.org/10.1109/TMECH.2021.3100537

Yoo YM, Kwon BI, 2007. A dual-servo type VCM for a nano-level measurement system. *J Electr Eng Technol*, 2(1):50-54. https://doi.org/10.5370/JEET.2007.2.1.050

Zhu HY, Teo TJ, Pang CK, 2018. Analytical model-based multi-physics optimization of a nanopositioning electromagnetic actuator. *IEEE Trans Ind Electron*, 65(1):478-487. https://doi.org/10.1109/TIE.2017.2714132

Zhu HY, Teo TJ, Pang CK, 2019. Magnetically levitated parallel actuated dual-stage (maglev-PAD) system for six-axis precision positioning. *IEEE/ASME Trans Mechatron*, 24(4): 1829-1838. https://doi.org/10.1109/TMECH.2019.2928978